Analysis of High-Fidelity Reduced-Order Linearized Time-Invariant Helicopter Models for Integrated Flight and On-Blade Control Applications

Ashwani K. Padthe
Peretz P. Friedmann
akpadthe@umich.edu
Department of Aerospace Engineering
University of Michigan
Ann Arbor, MI 48109
Ph : (734) 763-2354

Mark Lopez
J. V. R. Prasad
mlopez33@gatech.edu
School of Aerospace Engineering
Georgia Institute of Technology
Atlanta, GA 30332
Ph : (404) 894-3043

Abstract

Linearized time-periodic models are extracted from a high fidelity comprehensive nonlinear helicopter model at a low-speed descending flight as well as a cruise condition. A Fourier expansion based model reduction method is used to generate linearized time-invariant models from the time-periodic system. The linearized models, intended for studies examining the interaction between on-blade control and the primary flight control system, are very large in size with a few thousand states each. Therefore, a truncation method based on Hankel singular values is used to reduce the size of the LTI models. The reduced-order LTI models are then verified against the nonlinear model by comparing the hub load responses to an open-loop flap deflection. However, on-blade control is usually implemented in closed-loop mode, therefore, the reduced-order LTI models are verified for closed-loop performance fidelity. The higher harmonic controller is used with the 2/rev-5/rev harmonic components of the flap deflection as the control input and vibratory hub loads are the output. Closed-loop performance of the full-order LTI model, reduced-order LTI model, and the nonlinear model is compared at both the low-speed descending flight and the cruise flight conditions. The flap deflection histories and the vibratory loads predicted using the full-order and the reduced-order LTI models agree very well at both flight conditions when the flap deflection is limited to be less than 2°. The results show that the reduced-order LTI models capture all the relevant dynamics and are suitable for studying closed-loop on-blade vibration control and its interactions with the primary flight control system, as long as the dynamic stall effects are not significant.

Nomenclature

$\mathbf{A}(\psi), \mathbf{B}(\psi),$ $\mathbf{C}(\psi), \mathbf{E}(\psi)$	Matrices in the linear time-periodic model
$\mathbf{A}_{21}, \mathbf{A}_{22},$ $\mathbf{A}_{23}, \mathbf{A}_{31},$ $\mathbf{A}_{32}, \mathbf{A}_{33},$ $\mathbf{B}_2, \mathbf{B}_3, \mathbf{C}_2,$ $\mathbf{C}_3, \mathbf{E}_1$	Matrices in the linear time-invariant model
C_W	Helicopter weight coefficient
$\mathbf{D}_a$	$= -\frac{\partial \mathbf{h}_a}{\partial \dot{\mathbf{x}}_s}$
$\mathbf{D}_s$	$= -\frac{\partial \mathbf{h}}{\partial \dot{\mathbf{x}}_a}$
E	Root mean square error in the closed-loop flap deflection
$\mathbf{f}$	Output function relating the hub loads to the blade structural and aerodynamic degrees of freedom
f	Equivalent flat plate area of the fuselage
$\mathbf{h}$	Function representing blade structural equations of motion in terms of rotating coordinates
$\mathbf{h}_a$	Function representing blade aerodynamic

	equations of motion in terms of rotating coordinates
$\mathbf{G}_a$	$= \frac{\partial \mathbf{h}_a}{\partial \mathbf{u}}$
$\mathbf{G}_s$	$= \frac{\partial \mathbf{h}}{\partial \mathbf{u}}$
$\mathbf{g}$	Function representing blade structural equations of motion in terms of multiblade coordinates
$\mathbf{g}_a$	Function representing blade aerodynamic equations of motion in terms of multiblade coordinates
J	Vibratory cost function
$\mathbf{K}_{aa}$	$= -\frac{\partial \mathbf{h}_a}{\partial \mathbf{x}_a}$
$\mathbf{K}_{as}$	$= -\frac{\partial \mathbf{h}_a}{\partial \mathbf{x}_s}$
$\mathbf{K}_{sa}$	$= -\frac{\partial \mathbf{h}}{\partial \mathbf{x}_a}$
$\mathbf{K}_{ss}$	$= -\frac{\partial \mathbf{h}}{\partial \mathbf{x}_s}$
M_b	Blade mass
N_b	Number of rotor blades
$\mathbf{P}_a$	$= \frac{\partial \mathbf{f}}{\partial \mathbf{x}_a}$
$\mathbf{P}_s$	$= \frac{\partial \mathbf{f}}{\partial \mathbf{x}_s}$
$\mathbf{Q}$	$= \frac{\partial \mathbf{f}}{\partial \dot{\mathbf{x}}_s}$
$\mathbf{R}$	$= \frac{\partial \mathbf{f}}{\partial \ddot{\mathbf{u}}}$
R	Rotor blade radius
$\mathbf{u} = \{\mathbf{u}_1, \mathbf{u}_2, \mathbf{u}_3, \mathbf{u}_4\}'$	Individual blade coordinates representing flap deflection/control inputs
$\mathbf{u}_{\mathrm{aug}}$	Augmented input vector used in the LTI model
$\mathbf{x}_{\mathrm{aug}}$	Augmented state vector used in the LTI model
$\mathbf{u}_m = \{\mathbf{u}_{m0}, \mathbf{u}_{m1c}, \mathbf{u}_{m1s}, \mathbf{u}_{m2}\}'$	Multi-blade coordinates representing flap deflection/control inputs
X_{FA}, Z_{FA}	Longitudinal and vertical offsets between rotor hub and helicopter aerodynamic center
X_{FC}, Z_{FC}	Longitudinal and vertical offsets between rotor hub and helicopter center of gravity
$\mathbf{x}_s = \{\mathbf{x}_1, \mathbf{x}_2, \mathbf{x}_3, \mathbf{x}_4\}'$	Rotating blade coordinates representing blade deflections in the rotating coordinate system
$\mathbf{x}_a = \{\mathbf{x}_{a1}, \mathbf{x}_{a2}, \mathbf{x}_{a3}, \mathbf{x}_{a4}\}'$	Rotating blade coordinates representing the aerodynamic states in the rotating coordinate system
$\mathbf{x}_{ms} = \{\mathbf{x}_{m0}, \mathbf{x}_{m1c}, \mathbf{x}_{m1s}, \mathbf{x}_{m2}\}'$	Multi-blade coordinates representing blade deflections in the non-rotating coordinate system
$\mathbf{x}_{ma} = \{\mathbf{x}^a_{m0}, \mathbf{x}^a_{m1c}, \mathbf{x}^a_{m1s}, \mathbf{x}^a_{m2}\}'$	Multi-blade coordinates representing aerodynamic states in the non-rotating coordinate system
$\mathbf{x}^0_{m0}, \mathbf{x}^0_{m1c}, \mathbf{x}^0_{m1s}, \mathbf{x}^0_{m2}$	Multi-blade coordinates corresponding to the periodic equilibrium
$\mathbf{y}$	Output vector
$\mathbf{y}_{\mathrm{aug}}$	Augmented output vector used in the LTI model
α_{D}	Descent angle
β_p	Blade precone angle
γ	Lock number
δ	Flap or microflap deflection
Δ	Symbol indicating a perturbation
μ	Advance ratio
θ_{tw}	Blade pretwist distribution
σ	Rotor solidity
$\omega_F, \omega_L, \omega_T$	Blade flap, lag and torsional natural frequencies
Ω	Rotor angular speed
ψ	Azimuth angle
ζ	Output vector in the LTP model
ξ	State variable vector in the LTP model
υ	Input vector in the LTP model
$()^0$	Superscript indicating the average Fourier coefficient
$()^{ic}$	Superscript indicating the i^{th} cosine Fourier coefficient
$()^{is}$	Superscript indicating the i^{th} sine Fourier coefficient
ACF	Actively-Controlled Flaps
AVINOR	Active Vibration and Noise Reduction
DS	Dynamic Stall
FEMR	Fourier-Expansion based Model Reduction
HFC	Helicopter Flight Control
HHC	Higher Harmonic Control
LTI	Linear Time-Invariant
LTP	Linear Time-Periodic
OBC	On-Blade Control
RFA	Rational Function Approximation
RMS	Root Mean Square

1 Introduction

On-blade vibration reduction in rotorcraft has been an important area of research over the past three decades. In addition to causing crew and passenger discomfort, vibrations reduce the airframe and component fatigue life and limit rotorcraft performance resulting in high maintenance costs. On-blade active control (OBC) approaches, such as the actively controlled plain trailing-edge flaps (ACF) [1–3] and the microflaps [4] have been explored for rotorcraft vibration reduction. However, the influence of these OBC systems on the helicopter flight control systems (HFC) and its handling qualities has received attention only recently [5, 6]. Understanding and eliminating any adverse interaction between the high-bandwidth control using OBC systems and the closed-loop flight control systems is an essential pre-requisite to OBC implementation on a production helicopter.

The handling qualities specifications for small amplitude maneuvers prescribed in Aeronautical Design Standard (ADS-33, Ref. 7) are based on linear time-invariant (LTI) model specifications. Furthermore, LTI models provide a convenient framework for control system design. Thus, extraction of a LTI approximation of the helicopter dynamic model is an essential step towards carrying out an OBC and HFC interaction study. The first step in extraction of LTI models is to obtain a linearized time-periodic (LTP) model by linearizing the nonlinear model about a periodic equilibrium. Subsequently, LTI models are extracted from the LTP model. Various methods, such as the Lyapunov-Floquet transformation method, Hill's method, time-lifting and frequency-lifting methods have been explored in the literature [8] for reformulation of LTP models into LTI form. The Hill's method in which the LTI models are extracted using a Fourier expansion of the LTP model matrices has been found to provide a convenient framework for higher-harmonic control and flight control interaction studies in helicopters [5, 9, 10]. In Ref. 9, Hill's method was used to extract LTI helicopter model approximations capable of capturing N/rev vibratory hub load dynamics, where N is the number of rotor blades. Interactions between a conventional higher harmonic control (HHC) system and the HFC system were studied using the LTI helicopter models. The LTI models were extracted from an existing coupled nonlinear rotor-fuselage model of the Sikorsky UH-60 Black Hawk helicopter, where the blade model is based on the rigid flap-lag and first torsional degrees of freedom. Quasi-steady compressible aerodynamics and a three-state dynamic inflow model, which yields a linear inflow distribution over the rotor-disk were used in the nonlinear model. The conventional HHC controller was used to minimize the N/rev vibratory hub loads. Employing the HHC controller in a closed-loop mode had a negligible on HFC performance and handling qualities, implying lack of dynamic coupling between the two systems. However, pilot inputs to the HFC caused a significant change in the vibratory hub loads. Furthermore, the effectiveness of the HHC system in suppressing the transient vibratory response to pilot inputs was also examined. It was found that the root-mean-square of the vibratory shears was reduced by 30% compared to the baseline using a HHC system augmented with a second-order lead-lag compensator.

Another method for the extraction of LTI helicopter models from a nonlinear model was developed in Ref. 10. The method involves a two-step approach where a LTP model is extracted from a nonlinear model using a numerical perturbation scheme. Subsequently, a Fourier expansion based harmonic decomposition of the LTP model matrices is used to arrive at a LTI model of selected order. This method is refered to as the Fourier expansion based model reduction (FEMR) in this paper. The nonlinear helicopter model used in these studies was the generic helicopter model embedded in FLIGHTLAB that consists of a rigid flap mode, together with one elastic flap mode combined with rigid lead-lag mode for each blade. The blade feathering is assumed to be rigid and the aerodynamics are represented by a 15-state dynamic inflow model. These LTI models were later enhanced by adding elastic flap and lead-lag modes in Refs. 11 and 12, where an advanced control system based on dynamic crossfeeds that can mitigate the vibration response during a maneuvering flight was developed. The classical higher harmonic controller was used in this study. The nonlinear helicopter simulation models used in the studies mentioned above, due to lack of high fidelity aerodynamic models, can capture only the 1^{st} order dynamic effects, which are inadequate for accurate predictions of vibratory hub loads. Furthermore, the analyses considered the conventional HHC and individual blade control (IBC) but not any on-blade control systems. Recently, in Ref. 5, the FEMR approach was used to extract LTP and LTI models from a high fidelity nonlinear helicopter model embedded in the AVINOR (Active Vibration and Noise Reduction) code [13]. The nonlinear model accounts for higher-order structural dynamic effects, dynamic stall, non-uniform inflow, and unsteady aerodynamic effects due to on-blade control surfaces, providing an accurate prediction of the vibratory hub loads and the effects of on-blade control devices. The LTP and LTI model hub load responses were verified against the nonlinear model response. Very good agreement was obtained with the inclusion of the aerodynamic model states in the linearized models for prescribed open-loop flap inputs [5]. Recognizing that on-blade control devices are intended for a closed-loop mode of operation, the LTI models were also verified for closed-loop vibration reduction performance fidelity in Ref. 6. Good agreement was found between the LTI and nonlinear model predictions of the closed-loop flap deflection and vibration reduction performance.

The LTI models extracted in Refs. 5 and 6 were based on the first N/rev sine and cosine terms in the LTP state Fourier expansions. Thus, for every LTP state, the LTI model has 2N+1 states resulting in a system consisting of thousands of states. Working with such large models is not only computationally prohibitive but also inconvenient for control design. Therefore, it is necessary to reduce the LTI models to a reasonable size without compromising on the model fidelity. In this paper, a truncation method based on Hankel singular values is used to reduce the order of the LTI models. The hub load response of these reduced order models is then verified against the original full order model. Fidelity of the LTI models is evaluated at a low-speed descending flight condition and a cruise flight condition, where dynamic stall (DS) effects are present. The specific objectives of this paper are:

1. Construct high-fidelity LTP and LTI models that can accurately capture the closed-loop on-blade control characteristics of a nonlinear helicopter model.
2. Use Hankel singular values to reduce the LTI model order without compromising fidelity.
3. Verify the reduced order model response against the original model in both open-loop and closed-loop modes.
4. Evaluate the LTI model fidelity at various flight conditions including a high-speed cruise condition where significant DS effects are present.

2 Rotorcraft Aeroelastic Analysis Code

The AVINOR comprehensive rotorcraft aeroelastic response code, which has been extensively used to study vibration and noise reduction using flaps and microflaps [1, 4, 13], is employed in this study to extract linearized models. The principal ingredients of the AVINOR code are concisely summarized next.

2.1 Structural dynamic model

The geometrically nonlinear structural dynamic model in AVINOR accounts for moderate blade deflections and fully coupled flap-lag-torsional dynamics for each blade. The structural equations of motion are discretized using the global Galerkin method, using the free vibration modes of the rotating blade. The dynamics of the blade are represented by three flap, two lead-lag, and two torsional modes. The code also has the option of modeling the blades using a finite-element method. The effects of control surfaces such as the trailing-edge plain flaps on the structural properties of the blade are neglected. Thus, the control surfaces only influence the blade behavior through their effect on the aerodynamic and inertial loads.

2.2 Aerodynamic model

The blade/flap sectional time-domain aerodynamic loads for attached flow are calculated using a rational function approximation (RFA) based reduced order model constructed from frequency-domain doublet-lattice based aerodynamic data [14]. This model provides unsteady lift, moment, and hinge moment for the plain flap configurations. A more sophisticated CFD based RFA model that can predict drag in addition to lift, moment, and hinge moment due to flaps and microflaps is also available in the code. However, it is not used in this study because it is computationally more expensive. The RFA model is linked to a free wake model [15], which produces a spanwise and azimuthally varying inflow distribution. In the separated flow regime aerodynamic loads are calculated using the ONERA dynamic stall model [13].

2.3 Coupled aeroelastic response/trim solution

The combined structural and aerodynamic equations of motion are represented by a system of coupled ordinary differential equations with periodic coefficients in state-variable form. Propulsive trim, where three force equations (longitudinal, lateral, and vertical) and three moment equations (roll, pitch, and yaw) corresponding to a helicopter in free flight are enforced, is used. A simplified tail rotor model, based on uniform inflow and blade element theory, is employed. The six trim variables are the rotor shaft angle α_R, the collective pitch θ_0, the cyclic pitch θ_{1s} and θ_{1c}, the tail rotor constant pitch θ_{0t}, and lateral roll angle ϕ_R. The coupled trim/aeroelastic equations are solved in time using a predictor-corrector ODE solver DDEABM, based on the Adams-Bashforth direct numerical integration procedure.

2.4 The Higher Harmonic Control Algorithm

Active control of vibration and noise is implemented using the HHC algorithm, which has been used extensively in rotorcraft applications [15, 16]. The algorithm is based on the assumption that the helicopter can be represented by a linear model relating the output of interest $\mathbf{z}$ to the control input $\mathbf{u}$. The measurement of the plant output and update of the control input are performed at specific times $t_k = k\tau$, where τ is the time interval between updates during which the plant output reaches a steady state. A schematic of the HHC architecture implemented on a helicopter is shown in Fig. 1. The disturbance $\mathbf{w}$ represents the helicopter operating condition. The output vector at the k^{th} time step is given by

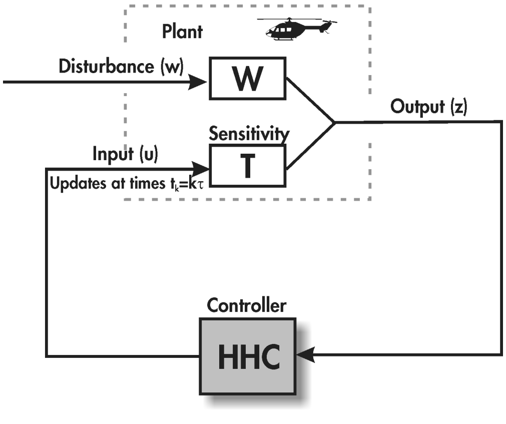

Figure 1: Higher harmonic control architecture

$$\mathbf{z}_k = \mathbf{T}\mathbf{u}_k + \mathbf{W}\mathbf{w} \tag{1}$$

where the sensitivity matrix $\mathbf{T}$ represents a linear approximation of the helicopter response to the control and is given by

$$\mathbf{T} = \frac{\partial \mathbf{z}}{\partial \mathbf{u}}. \tag{2}$$

At the initial condition, $k = 0$,

$$\mathbf{z}_0 = \mathbf{T}\mathbf{u}_0 + \mathbf{W}\mathbf{w}. \tag{3}$$

Subtracting Eq. (3) from Eq. (1) to eliminate the unknown $\mathbf{w}$ yields

$$\mathbf{z}_k = \mathbf{z}_0 + \mathbf{T}(\mathbf{u}_k - \mathbf{u}_0). \tag{4}$$

Another version of Eq. (4) where subsequent control updates are used

$$\mathbf{z}_{k+1} = \mathbf{z}_k + \mathbf{T}(\mathbf{u}_{k+1} - \mathbf{u}_k), \tag{5}$$

is refered to as the recursive version. The controller is based on the minimization of a quadratic cost function

$$J(\mathbf{z}_{k+1}, \mathbf{u}_{k+1}) = \mathbf{z}_{k+1}^{\mathrm{T}}\mathbf{Q}\mathbf{z}_{k+1} + \mathbf{u}_{k+1}^{\mathrm{T}}\mathbf{R}\mathbf{u}_{k+1}. \tag{6}$$

The optimal control input is determined from the requirement

$$\frac{\partial J(\mathbf{z}_k, \mathbf{u}_k)}{\partial \mathbf{u}_k} = 0. \tag{7}$$

Minimization with respect to $\mathbf{u}_{k+1}$ yields the optimal control input

$$\mathbf{u}_{k+1,\mathrm{opt}} = -(\mathbf{T}^{\mathrm{T}}\mathbf{Q}\mathbf{T}+\mathbf{R})^{-1}(\mathbf{T}^{\mathrm{T}}\mathbf{Q})(\mathbf{z}_k - \mathbf{T}\mathbf{u}_k). \tag{8}$$

This is a classical version of the HHC algorithm that yields an explicit relation for the optimal control input. Another version of the HHC algorithm where the sensitivity matrix $\mathbf{T}$ is updated using least-squares methods after every control update is known as the adaptive HHC and is discussed in Ref. 16.

In a 4-bladed rotor, the control input $\mathbf{u}_k$ is a combination of 2/rev, 3/rev, 4/rev, and 5/rev harmonic amplitudes of the control surface deflection:

$$\mathbf{u}_k = [\delta_{2c}, \delta_{2s}, ..., \delta_{5c}, \delta_{5s}]^T. \tag{9}$$

The total control surface deflection is given by

$$\delta(\psi, \mathbf{u}_k) = \sum_{N=2}^{5} \left[\delta_{Nc}\cos(N\psi) + \delta_{Ns}\sin(N\psi)\right]. \tag{10}$$

where the quantities δ_{Nc} and δ_{Ns} correspond to the cosine and sine components of the N/rev control input harmonic. For vibration reduction (VR) studies, the output vector $\mathbf{z}_k$ consists of 4/rev vibratory hub shears and moments:

$$\mathbf{z}_{\text{VR}} = \begin{bmatrix} F_{HX4} \\ F_{HY4} \\ F_{HZ4} \\ M_{HX4} \\ M_{HY4} \\ M_{HZ4} \end{bmatrix}. \tag{11}$$

The weighting matrix $\mathbf{Q}$ in the cost function in Eq. 6 is a diagonal matrix. For vibration control, it is described by six weights corresponding to the three vibratory hub shears and the three vibratory hub moments.

3 LTP and LTI model extraction from AVINOR

The procedure for extracting linearized time-periodic and time-invariant models from the nonlinear AVINOR code is briefly described in this section. Details of the extraction procedure can be found in Ref. 5. First, a LTP model is extracted by linearizing the nonlinear model about a trim state. Steps implemented are outlined in Fig. 2. The first box represents the structural equations of motion in the AVINOR code formulated as

$$\ddot{\mathbf{x}}_s = \mathbf{h}(\mathbf{x}_s, \dot{\mathbf{x}}_s, \mathbf{x}_a, \mathbf{u}) \tag{12}$$

where $\mathbf{x}_s$ is the state variable vector containing the structural degrees of freedom, $\mathbf{x}_a$ is the state variable vector containing the augmented aerodynamic states associated with the RFA aerodynamic model [14], $\mathbf{u}$ is the control input vector, and $\mathbf{h}$ is a general nonlinear function. The first step in the linearization procedure as represented in the second box in Fig. 2 is to linearize Eq. (12) about a periodic equilibrium, which yields a linear time-periodic system given by

$$\begin{aligned}\Delta\ddot{\mathbf{x}}_s =& \frac{\partial \mathbf{h}}{\partial \mathbf{x}_s}(\psi)\Delta\mathbf{x}_s + \frac{\partial \mathbf{h}}{\partial \dot{\mathbf{x}}_s}(\psi)\Delta\dot{\mathbf{x}}_s + \frac{\partial \mathbf{h}}{\partial \mathbf{x}_a}(\psi)\Delta\mathbf{x}_a \\ &+ \frac{\partial \mathbf{h}}{\partial \mathbf{u}}(\psi)\Delta\mathbf{u}\end{aligned} \tag{13}$$

or

$$\begin{aligned}\Delta\ddot{\mathbf{x}}_s =& -\mathbf{K}_{ss}(\psi)\Delta\mathbf{x}_s - \mathbf{K}_{sa}(\psi)\Delta\mathbf{x}_a - \mathbf{D}_s(\psi)\Delta\dot{\mathbf{x}}_s \\ &+ \mathbf{G}_s(\psi)\Delta\mathbf{u}\end{aligned} \tag{14}$$

where $\Delta\mathbf{x}_s, \Delta\dot{\mathbf{x}}_s, \Delta\mathbf{x}_a, \Delta\mathbf{u}$ represent perturbations in $\mathbf{x}_s, \dot{\mathbf{x}}_s, \mathbf{x}_a, \mathbf{u}$, respectively. The derivatives $\mathbf{K}_{ss}(\psi)$, $\mathbf{D}_s(\psi)$, $\mathbf{K}_{sa}(\psi)$, and $\mathbf{G}_s(\psi)$ are matrix functions dependent on the azimuthal angle ψ and are calculated at a finite number of azimuthal steps (in the current study, 320 equally spaced steps are used in a revolution) using a central differencing scheme given as

$$\frac{\partial \mathbf{h}}{\partial \mathbf{x}_s} \approx \frac{\mathbf{h}(\bar{\mathbf{x}}_s + \Delta\mathbf{x}_s, \dot{\bar{\mathbf{x}}}_s, \bar{\mathbf{x}}_a, \bar{\mathbf{u}}) - \mathbf{h}(\bar{\mathbf{x}}_s - \Delta\mathbf{x}_s, \dot{\bar{\mathbf{x}}}_s, \bar{\mathbf{x}}_a, \bar{\mathbf{u}})}{2\Delta\mathbf{x}_s} \tag{15}$$

$$\frac{\partial \mathbf{h}}{\partial \dot{\mathbf{x}}_s} \approx \frac{\mathbf{h}(\bar{\mathbf{x}}_s, \dot{\bar{\mathbf{x}}}_s + \Delta\dot{\mathbf{x}}_s, \bar{\mathbf{x}}_a, \bar{\mathbf{u}}) - \mathbf{h}(\bar{\mathbf{x}}_s, \dot{\bar{\mathbf{x}}}_s - \Delta\dot{\mathbf{x}}_s, \bar{\mathbf{x}}_a, \bar{\mathbf{u}})}{2\Delta\dot{\mathbf{x}}_s} \tag{16}$$

$$\frac{\partial \mathbf{h}}{\partial \mathbf{x}_a} \approx \frac{\mathbf{h}(\bar{\mathbf{x}}_s, \dot{\bar{\mathbf{x}}}_s, \bar{\mathbf{x}}_a + \Delta\mathbf{x}_a, \bar{\mathbf{u}}) - \mathbf{h}(\bar{\mathbf{x}}_s, \dot{\bar{\mathbf{x}}}_s, \bar{\mathbf{x}}_a - \Delta\mathbf{x}_a, \bar{\mathbf{u}})}{2\Delta\mathbf{x}_a} \tag{17}$$

$$\frac{\partial \mathbf{h}}{\partial \mathbf{u}} \approx \frac{\mathbf{h}(\bar{\mathbf{x}}_s, \dot{\bar{\mathbf{x}}}_s, \bar{\mathbf{x}}_a, \bar{\mathbf{u}} + \Delta\mathbf{u}) - \mathbf{h}(\bar{\mathbf{x}}_s, \dot{\bar{\mathbf{x}}}_s, \bar{\mathbf{x}}_a, \bar{\mathbf{u}} - \Delta\mathbf{u})}{2\Delta\mathbf{u}} \tag{18}$$

where $(\bar{\mathbf{x}}_s, \dot{\bar{\mathbf{x}}}_s, \bar{\mathbf{x}}_a, \bar{\mathbf{u}})$ represents a periodic eqilibrium condition. This step is represented in the third and fourth blocks in Fig. 2.

The differential equations corresponding to the RFA aerodynamic model in the AVINOR code can be represented as

$$\dot{\mathbf{x}}_a = \mathbf{h}_a(\mathbf{x}_s, \dot{\mathbf{x}}_s, \mathbf{x}_a, \mathbf{u}). \tag{19}$$

Linearization about a periodic equilibrium yields

$$\begin{aligned}\Delta\dot{\mathbf{x}}_a =& \frac{\partial \mathbf{h}_a}{\partial \mathbf{x}_s}(\psi)\Delta\mathbf{x}_s + \frac{\partial \mathbf{h}_a}{\partial \dot{\mathbf{x}}_s}(\psi)\Delta\dot{\mathbf{x}}_s + \frac{\partial \mathbf{h}_a}{\partial \mathbf{x}_a}(\psi)\Delta\mathbf{x}_a \\ &+ \frac{\partial \mathbf{h}_a}{\partial \mathbf{u}}(\psi)\Delta\mathbf{u},\end{aligned} \tag{20}$$

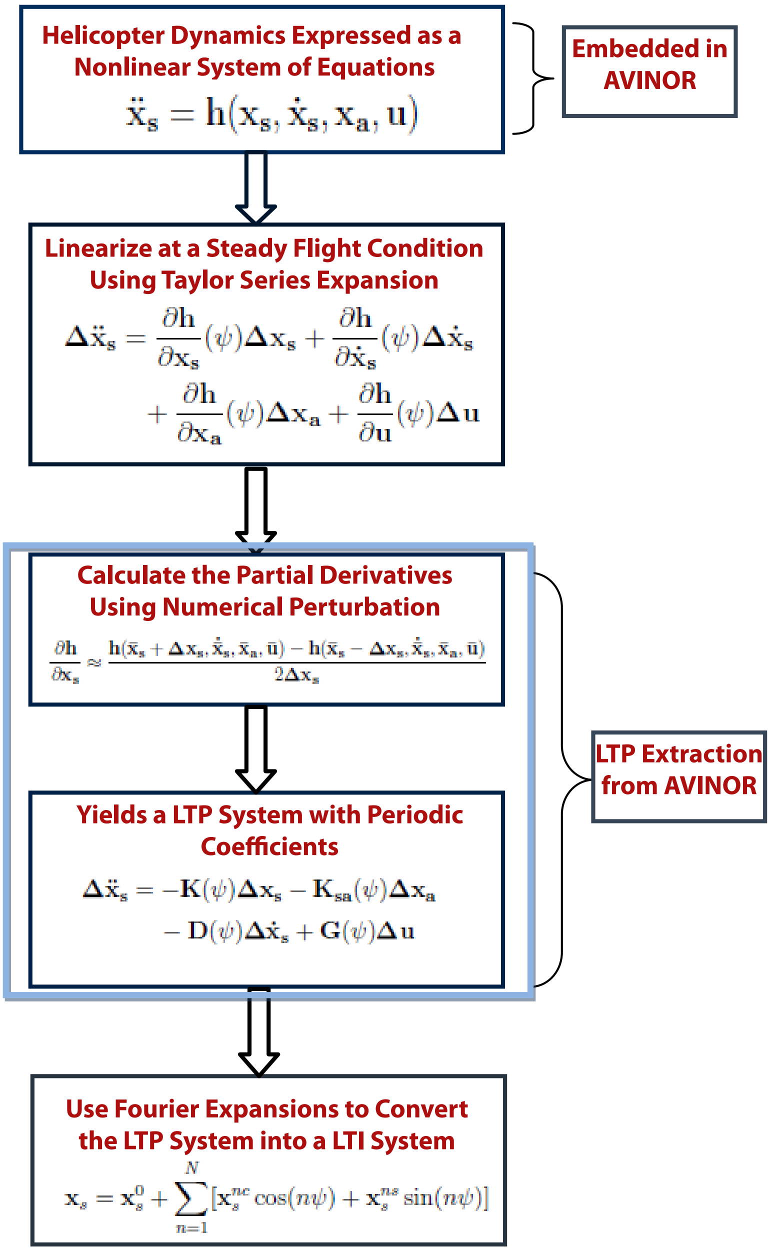

Figure 2: A schematic of the steps involved in extracting linearized models from AVINOR.

or

$$\Delta\dot{\mathbf{x}}_a = -\mathbf{K}_{as}(\psi)\Delta\mathbf{x}_s - \mathbf{K}_{aa}(\psi)\Delta\mathbf{x}_a - \mathbf{D}_a(\psi)\Delta\dot{\mathbf{x}}_s + \mathbf{G}_a(\psi)\Delta\mathbf{u}, \tag{21}$$

where the derivatives $\mathbf{K}_{as}(\psi)$, $\mathbf{D}_a(\psi)$, $\mathbf{K}_{aa}(\psi)$, and $\mathbf{G}_a(\psi)$ represent the effect of perturbations in the various state variables and control inputs on the aerodynamic state derivatives. A similar linearization procedure is adopted for the output equation. In this study the vibratory hub loads are chosen as the output quantities. The vibratory hub shears and moments are obtained from the integration of the distributed inertial and aerodynamic loads over the entire blade span. This relation can be represented by a nonlinear function

$$\mathbf{y} = \mathbf{f}(\mathbf{x}_s, \dot{\mathbf{x}}_s, \mathbf{x}_a, \mathbf{u}), \tag{22}$$

and is linearized about a periodic equilibrium. The linearized equation is expressed as

$$\Delta\mathbf{y} = \frac{\partial\mathbf{f}}{\partial\mathbf{x}_s}(\psi)\Delta\mathbf{x}_s + \frac{\partial\mathbf{f}}{\partial\dot{\mathbf{x}}_s}(\psi)\Delta\dot{\mathbf{x}}_s + \frac{\partial\mathbf{f}}{\partial\mathbf{x}_a}(\psi)\Delta\mathbf{x}_a + \frac{\partial\mathbf{f}}{\partial\mathbf{u}}(\psi)\Delta\mathbf{u}, \tag{23}$$

or

$$\Delta\mathbf{y} = \mathbf{P}_s(\psi)\Delta\mathbf{x}_s + \mathbf{Q}(\psi)\Delta\dot{\mathbf{x}}_s + \mathbf{P}_a(\psi)\Delta\mathbf{x}_a + \mathbf{R}(\psi)\Delta\mathbf{u}. \tag{24}$$

The partial derivatives $\mathbf{P}_s(\psi)$, $\mathbf{P}_a(\psi)$, $\mathbf{Q}(\psi)$, and $\mathbf{R}(\psi)$ represent the change in the vibratory loads due to a unit perturbation in the state variables, their derivatives, and the control inputs, respectively. The central differencing scheme is used to evaluate all the partial derivatives in this study. The final LTP representation of the helicopter model expressed in a state space form is:

$$\dot{\xi} = \mathbf{A}(\psi)\xi + \mathbf{B}(\psi)\upsilon \tag{25}$$

$$\zeta = \mathbf{C}(\psi)\xi + \mathbf{E}(\psi)\upsilon \tag{26}$$

where

$$\begin{aligned}
\xi &= [\Delta\mathbf{x}_s \quad \Delta\mathbf{x}_a \quad \Delta\dot{\mathbf{x}}_s]^T,\\
\upsilon &= [\Delta\mathbf{u}]^T,\\
\zeta &= [\Delta\mathbf{y}]^T,\\
\mathbf{A}(\psi) &= \begin{bmatrix} \mathbf{0} & \mathbf{0} & \mathbf{I} \\ -\mathbf{K}_{as}(\psi) & -\mathbf{K}_{aa}(\psi) & -\mathbf{D}_a(\psi) \\ -\mathbf{K}_{ss}(\psi) & -\mathbf{K}_{sa}(\psi) & -\mathbf{D}(\psi) \end{bmatrix},\\
\mathbf{B}(\psi) &= \begin{bmatrix} \mathbf{0} \\ \mathbf{G}_a(\psi) \\ \mathbf{G}_s(\psi) \end{bmatrix},\\
\mathbf{C}(\psi) &= [\mathbf{P}_s(\psi) \quad \mathbf{P}_a(\psi) \quad \mathbf{Q}(\psi)],\\
\mathbf{E}(\psi) &= [\mathbf{R}(\psi)].
\end{aligned}$$

Linearized models extracted in this study will be used to examine interactions between on-blade control and the flight control systems. In order to study coupled rotor-fuselage dynamics of a helicopter, it is convenient to describe the rotating blade motion in a non-rotating coordinate system. Multiblade coordinates (MBC) are widely used in the literature to express the blade motion in the non-rotating coordinate system [17]. The blade equations of motion in AVINOR are solved in the rotating frame using rotating blade coordinates (RBC). Therefore, when extracting the linearized models from AVINOR, a coordinate transformation is used to transform the blade degrees of freedom from RBC to MBC. For a 4-bladed rotor, the MBC transformation expressed in terms of the rotating blade coordinates is:

$$x_{m0} = \frac{1}{4}\sum_{n=1}^{4} x_n \tag{27}$$

$$x_{m1c} = \frac{1}{2}\sum_{n=1}^{4} x_n \cos\psi_n \tag{28}$$

$$x_{m1s} = \frac{1}{2}\sum_{n=1}^{4} x_n \sin\psi_n \tag{29}$$

$$x_{m2} = \frac{1}{4}\sum_{n=1}^{4} (-1)^n x_n \tag{30}$$

where $x_{m0}, x_{m1c}, x_{m1s}, x_{m2}$ are the collective, cosine, sine, and differential multi-blade coordinates, respectively, and x_n and ψ_n are the individual blade coordinate and azimuth angle corresponding to the n^{th} blade, respectively. For a 4-bladed rotor, the individual blade coordinate of the nth blade is given in terms of MBC as:

(31)

$$x_n = x_{m0} + x_{m1c}\cos\psi_n + x_{m1s}\sin\psi_n + (-1)^n x_{m2}.$$

Similar transformations are defined for the control inputs. The implementation of these transformations to generate a linearized helicopter system of equations in terms of MBC is provided in Ref. 5.

The FEMR approach [10] is used to extract LTI models from the LTP models (Eqs. (25), (26)). As represented by the last box in Fig. 2, this approach is based on a Fourier approximation to the state, output and input variables $\Delta\mathbf{x}_s$, $\Delta\mathbf{x}_a$, $\Delta\mathbf{u}$, and $\Delta\mathbf{y}$, given as:

(32)

$$\Delta\mathbf{x}_s = \Delta\mathbf{x}_s^0 + \sum_{n=1}^{N}[\Delta\mathbf{x}_s^{nc}\cos(n\psi) + \Delta\mathbf{x}_s^{ns}\sin(n\psi)],$$

(33)

$$\Delta\mathbf{x}_a = \Delta\mathbf{x}_a^0 + \sum_{n=1}^{N}[\Delta\mathbf{x}_a^{nc}\cos(n\psi) + \Delta\mathbf{x}_a^{ns}\sin(n\psi)],$$

(34)

$$\Delta\mathbf{u} = \Delta\mathbf{u}^0 + \sum_{m=1}^{M}[\Delta\mathbf{u}^{mc}\cos(m\psi) + \Delta\mathbf{u}^{ms}\sin(m\psi)],$$

(35)

$$\Delta\mathbf{y} = \Delta\mathbf{y}^0 + \sum_{l=1}^{L}[\Delta\mathbf{y}^{lc}\cos(n\psi) + \Delta\mathbf{y}^{ls}\sin(l\psi)].$$

where $\Delta\mathbf{x}_s^0, \Delta\mathbf{x}_a^0, \Delta\mathbf{u}_0, \Delta\mathbf{y}_0$ are the average components, $\Delta\mathbf{x}_s^{nc}, \Delta\mathbf{x}_a^{nc}, \Delta\mathbf{u}^{mc}, \Delta\mathbf{y}^{lc}$ are the cosine harmonic components, and $\Delta\mathbf{x}_s^{ns}, \Delta\mathbf{x}_a^{ns}, \Delta\mathbf{u}^{ms}, \Delta\mathbf{y}^{ls}$ are the sine harmonic components. Differentiating the expansion for $\Delta\mathbf{x}_s$ and $\Delta\mathbf{x}_a$ with respect to ψ,

(36)

$$\begin{aligned}\Delta\dot{\mathbf{x}}_s = \Delta\dot{\mathbf{x}}_s^0 + \sum_{n=1}^{N}[&(\Delta\dot{\mathbf{x}}_s^{nc} + n\Delta\mathbf{x}_s^{ns})\cos(n\psi)\\ &+ (\Delta\dot{\mathbf{x}}_s^{ns} - n\Delta\mathbf{x}_s^{nc})\sin(n\psi)],\end{aligned}$$

(37)

$$\begin{aligned}\Delta\dot{\mathbf{x}}_a = \Delta\dot{\mathbf{x}}_a^0 + \sum_{n=1}^{N}[&(\Delta\dot{\mathbf{x}}_a^{nc} + n\Delta\mathbf{x}_a^{ns})\cos(n\psi)\\ &+ (\Delta\dot{\mathbf{x}}_a^{ns} - n\Delta\mathbf{x}_a^{nc})\sin(n\psi)].\end{aligned}$$

Differentiating the structural equation again yields

(38)

$$\begin{aligned}\Delta\ddot{\mathbf{x}}_s = \Delta\ddot{\mathbf{x}}_s^0 + \sum_{n=1}^{N}[&(\Delta\ddot{\mathbf{x}}_s^{nc} + 2n\Delta\dot{\mathbf{x}}_s^{ns} - n^2\Delta\mathbf{x}_s^{nc})\cos(n\psi)\\ &+ (\Delta\ddot{\mathbf{x}}_s^{ns} - 2n\Delta\dot{\mathbf{x}}_s^{nc} - n^2\Delta\mathbf{x}_s^{ns})\sin(n\psi)].\end{aligned}$$

Fourier expansions are also defined for the system matrices, for example,

(39)

$$\mathbf{K}_{ss}(\psi) = \mathbf{K}_{ss}^0 + \sum_{n=1}^{N}[\mathbf{K}_{ss}^{nc}\cos(n\psi) + \mathbf{K}_{ss}^{ns}\sin(n\psi)],$$

where

$$\begin{aligned}\mathbf{K}_{ss}^0 &= \frac{1}{2\pi}\int_0^{2\pi}\mathbf{K}_{ss}(\psi)d\psi,\\ \mathbf{K}_{ss}^{ic} &= \frac{1}{\pi}\int_0^{2\pi}\mathbf{K}_{ss}(\psi)\cos(i\psi)d\psi,\\ \mathbf{K}_{ss}^{is} &= \frac{1}{\pi}\int_0^{2\pi}\mathbf{K}_{ss}(\psi)\sin(i\psi)d\psi.\\ &i = 1, 2, \ldots, N\end{aligned}$$

Substituting Eqs. (32)-(34), (36), and (38) into the blade structural equation of motion, Eq. (14) yields,

(40)

$$\begin{aligned}&\Delta\ddot{\mathbf{x}}_s^0 + \sum_{i=1}^{N}[(\Delta\ddot{\mathbf{x}}_s^{ic} + 2i\Delta\dot{\mathbf{x}}_s^{is} - i^2\Delta\mathbf{x}_s^{ic})\cos(i\psi)\\ &\qquad + (\Delta\ddot{\mathbf{x}}_s^{is} - 2i\Delta\dot{\mathbf{x}}_s^{ic} - i^2\Delta\mathbf{x}_s^{is})\sin(i\psi)]\\ &= -\mathbf{K}_{ss}(\psi)\left\{\Delta\mathbf{x}_s^0 + \sum_{n=1}^{N}[\Delta\mathbf{x}_s^{nc}\cos(n\psi) + \Delta\mathbf{x}_s^{ns}\sin(n\psi)]\right\}\\ &- \mathbf{K}_{sa}(\psi)\left\{\Delta\mathbf{x}_a^0 + \sum_{n=1}^{N}[\Delta\mathbf{x}_a^{nc}\cos(n\psi) + \Delta\mathbf{x}_a^{ns}\sin(n\psi)]\right\}\\ &- \mathbf{D}_s(\psi)\left\{\Delta\dot{\mathbf{x}}_s^0 + \sum_{n=1}^{N}[(\Delta\dot{\mathbf{x}}_s^{nc} + n\Delta\mathbf{x}_s^{ns})\cos(n\psi)\right.\\ &\qquad\qquad \left. + (\Delta\dot{\mathbf{x}}_s^{ns} - n\Delta\mathbf{x}_s^{nc})\sin(n\psi)]\right\}\\ &+ \mathbf{G}_s(\psi)\left\{\Delta\mathbf{u}^0 + \sum_{m=1}^{M}[\Delta\mathbf{u}^{mc}\cos(m\psi) + \Delta\mathbf{u}^{ms}\sin(m\psi)]\right\}\end{aligned}$$

Equation for the average component $\mathbf{x}_s^0$ is obtained by applying $\frac{1}{2\pi}\int_0^{2\pi}$ averaging procedure to both sides of Eq. (40). Equation for the i^{th} harmonic cosine component $\Delta\mathbf{x}_s^{ic}$ can be obtained by multiplying both sides of Eq. (40) by $\frac{1}{\pi}\cos(i\psi)$ and integrating it over one revolution. In a similar manner, the equation for the i^{th} harmonic sine component $\Delta\mathbf{x}_s^{is}$ can be obtained by multiplying both sides of Eq. (40) by $\frac{1}{\pi}\sin(i\psi)$ and integrating it over one revolution. Performing similar operations on the aerodynamic state equation and the output equation, and defining augmented state, input, and output vectors as

$$\begin{aligned}
\mathbf{x}_{\text{aug}} &= [\mathbf{x}_s^0 \ldots \mathbf{x}_s^{nc} \quad \mathbf{x}_s^{ns} \ldots \dot{\mathbf{x}}_s^0 \ldots \dot{\mathbf{x}}_s^{nc} \quad \dot{\mathbf{x}}_s^{ns} \ldots \\
&\qquad\qquad \ldots \mathbf{x}_a^0 \ldots \mathbf{x}_a^{nc} \quad \mathbf{x}_a^{ns} \ldots]^T, \\
\mathbf{u}_{\text{aug}} &= [\mathbf{u}^0 \ldots \mathbf{u}^{mc} \quad \mathbf{u}^{ms} \ldots]^T, \\
\mathbf{y}_{\text{aug}} &= [\mathbf{y}^0 \ldots \mathbf{y}^{lc} \quad \mathbf{y}^{ls} \ldots]^T,
\end{aligned}$$

the linear equations can be consolidated and expressed as a state-space LTI model given by

(41)

$$\dot{\mathbf{x}}_{\text{aug}} = \begin{bmatrix} \mathbf{0} & \mathbf{0} & \mathbf{I} \\ \mathbf{A}_{21} & \mathbf{A}_{22} & \mathbf{A}_{23} \\ \mathbf{A}_{31} & \mathbf{A}_{32} & \mathbf{A}_{33} \end{bmatrix} \mathbf{x}_{\text{aug}} + \begin{bmatrix} \mathbf{0} \\ \mathbf{B}_2 \\ \mathbf{B}_3 \end{bmatrix} \mathbf{u}_{\text{aug}},$$

(42)

$$\mathbf{y}_{\text{aug}} = [\mathbf{C}_1 \quad \mathbf{C}_2 \quad \mathbf{C}_3]\,\mathbf{x}_{\text{aug}} + \mathbf{E}_1\mathbf{u}_{\text{aug}},$$

where the matrices $\mathbf{A}_{21}$, $\mathbf{A}_{22}$, $\mathbf{A}_{23}$, $\mathbf{A}_{31}$, $\mathbf{A}_{32}$, $\mathbf{A}_{33}$, $\mathbf{B}_2$, $\mathbf{B}_3$, $\mathbf{C}_1$, $\mathbf{C}_2$, $\mathbf{C}_3$, and $\mathbf{E}_1$ are derived in Ref. 5.

4 Model Order Reduction

The LTI models used in the previous studies [5,6] retained up to N/rev sine and cosine terms in the Fourier expansion of the LTP states. Thus, corresponding to every state in the LTP model, the LTI model has 2N+1 states resulting in a system containing a few thousand states. The large size of the system diminishes computational efficiency and does not lend itself to control design. Therefore, it is necessary to reduce the size of the LTI model without compromising its fidelity. A method for model order reduction based on the modal participation of the various states is discussed in Ref. 18. The order reduction uses a comparison of the modal participation factor in the LTI and LTP models, for reducing the size of the LTI model. Two different metrics, namely, error as additive uncertainty and gap-metric analysis, were described to quantify the fidelity of the reduced-order models. However, the method has several shortcomings. It has limitations for $\mu < 0.30$ due to repeated eigenvalues. Furthermore, it is suitable for applications where in addition to the input-output relations, the system states are also of interest. This is not the case for vibration reduction using on-blade flap deflection where only the input-output relation is required. Furthermore, all the studies in this paper are conducted for $\mu \leq 0.35$. Therefore, the modal participation based method is not suitable. In the current study, the LTI model size reduction is implemented using the balanced model reduction method [12, 19]. A balanced realization of a LTI system is one for which the controllability and observability Gramians are equal and diagonal. The diagonal elements of the Gramian matrices of a balanced realization are refered to as the Hankel singular values. These values represent the "energy" associated with the LTI model states and consequently their influence on the system stability and response. The LTI model size is reduced by truncating the states having relatively low Hankel Singular Values. The MATLAB functions *hsvd* and *balred* are used to calculate the Hankel singular values and subsequently produce a reduced-order model.

5 Closed-loop Control Using LTI Models

On-blade control devices are implemented in closed-loop mode for rotorcraft vibration reduction. Therefore, to accurately study on-blade control and flight control interactions, it is imperative that the LTI models retain the closed-loop characteristics of the nonlinear model. In order to evaluate the closed-loop fidelity of the reduced-order LTI models, extracted using the procedure described in the previous sections, closed-loop performance of the on-blade control devices predicted using the LTI models is compared to that predicted using the nonlinear model. Specifically, the optimal flap deflection predictions and the reduction in vibratory hub loads are compared. An illustration of on-blade vibration control with the LTI helicopter model and the HHC controller implemented in a feedback loop is shown in Fig. 3. The LTI models predict only perturbations in the vibratory hub loads due to flap deflection. Therefore, the steady state hub loads are added to the LTI model predictions to obtain the complete vibratory loads. Then, a Fourier transform is used to extract the 4/rev components of the vibratory loads, which in turn are fed into the higher harmonic controller. The classical HHC controller is used to determine the optimal control input for vibratory load reduction. An adaptive version of the algorithm is not necessary when working with LTI

Table 1: Rotor configuration parameters used.

Dimensional Rotor Data	
R = 4.91 m	
M_b = 27.35 kg	
Ω = 425 RPM	
Nondimensional Rotor Data	
$N_b = 4$	$L_b = 1.0$
$c/R = 0.05498$	θ_{tw} = -8°
$e = 0$	
$X_A = 0$	$X_{Ib} = 0$
ω_F = 1.124, 3.40, 7.60	ω_L = 0.732, 4.458
ω_T = 3.17, 9.08	
$\gamma = 5.5$	$\sigma = 0.07$
β_p = 2.5°	
Helicopter Data	
$C_W = 0.005$	$fC_{df} = 0.031$
$X_{FA} = 0.0$	$Z_{FA} = 0.3$
$X_{FC} = 0.0$	$Z_{FC} = 0.3$

helicopter models. The control input is a combination of the 2/rev, 3/rev, 4/rev, and 5/rev harmonic components of the flap deflection. The sensitivity matrix **T**, used in the HHC algorithm, is also obtained from the LTI model. A comparison of the **T** matrices obtained from the nonlinear and the LTI models revealed negligible differences. This can be attributed to the fact that small flap deflection perturbation values were used to obtain the **T** matrices.

6 Results and Discussion

The rotor configuration considered is a four-bladed hingeless rotor, resembling the BO-105 type rotor; the rotor parameters are listed in Table 1. All the values in the table (except C_W, γ, and σ) have been nondimensionalized using M_b, L_b, and $1/\Omega$ for mass, length and time, respectively. The spanwise mass and stiffness distributions are assumed to be constant. All the blades are assumed to be identical. The rotor is trimmed using a propulsive trim procedure.

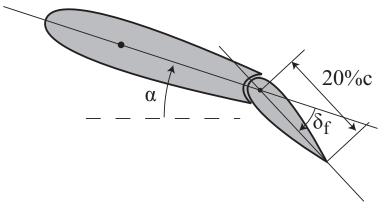

Figure 4: A 20%c conventional plain flap configuration.

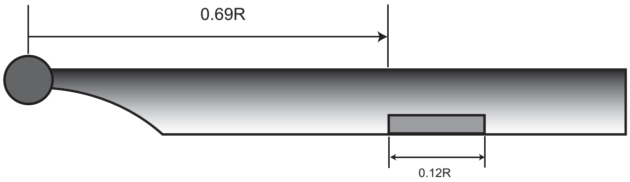

Figure 5: Spanwise configuration of the 20%c plain flap on the rotor blade.

Linearized time-periodic and time-invariant models were extracted from the AVINOR code at two different flight conditions. A steady descending flight condition with advance ratio $\mu = 0.15$ and descent angle $\alpha_{\text{D}} = 6.5°$, which represents heavy BVI conditions and cruise flight condition at advance ratio $\mu = 0.35$. A single plain flap with a 20% chord length, shown in Fig. 4, is used for active control. The flap is centered at 75% span location and its spanwise length is 12% of the blade radius as shown in Fig. 5. The LTP model is based on 7 states corresponding to the blade structural degrees of freedom (3 flap, 2 lead-lag, and 2 torsional), 7 states corresponding to their derivatives, and 100 states corresponding to the RFA aerodynamic model. The reason for the large number of aerodynamic states is that the state-space RFA model is used to predict the 2-dimensional lift, moment, and hinge moment at several spanwise stations on the blade. Therefore, the LTP model has 456 (114*4) states when modeled using the multi-blade coordinates. The AVINOR code does not account for the body degrees of freedom. In order to study the effect of active vibration control on the flight handling qualities, the body degrees of freedom have to be present in linear models. This issue will be addressed in future studies. A rotor revolution is divided into 320 azimuthal steps in order to calculate the LTP model matrices $A(\psi)$, $B(\psi)$, $C(\psi)$, and $E(\psi)$. A trial and error procedure was used to determine the optimum perturbation values. A 10% perturbation is used for the structural and aerodynamic states and a 0.25° perturbation is used for the flap deflection in LTP model extraction. The flap deflection control input in the AVINOR code is specified in the frequency domain through the harmonic component amplitudes. In order to specify a constant perturbation in flap deflection, during LTP model extraction, the cosine 0/rev component is set to 0.25° and all the other

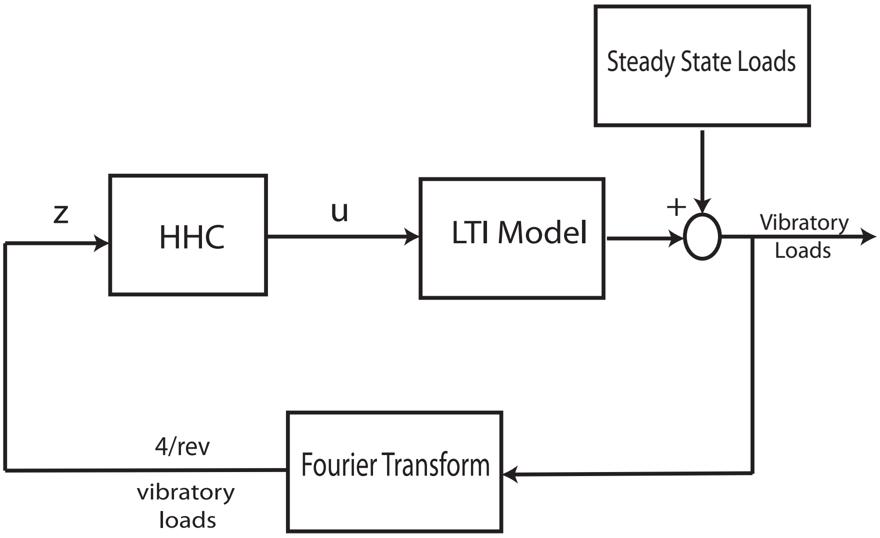

Figure 3: An illustration of closed-loop on-blade vibration control using a LTI helicopter model and the HHC controller.

components are set to 0. This is an artificial way to specify a constant flap deflection using harmonic component amplitudes. Consequently, the effects of flap deflection rate ($\dot{u}$) are neglected. For the LTI model extraction, the average component and the first 4 cosine and sine components are retained in the Fourier expansion. In a previous study [5] it was shown that the first 4 harmonic components of the Fourier expansion are sufficient for capturing all the important dynamics in the LTP model. Therefore, the LTI model has a total of 4104 (456*9) states. The linearized models were verified in Ref. 5 by comparing their output response with the nonlinear model response corresponding to a *open-loop* higher harmonic flap deflection. Subsequently, the *closed-loop* fidelity of the LTI models used during vibratory hub load reduction was verified in Ref. 6.

As mentioned above, these LTI models retain up to N/rev sine and cosine terms in the Fourier expansion of the LTP states resulting in over 4000 states. Such large size is computationally prohibitive and also inconvenient for control design. Therefore, the balanced model reduction method, described in a previous section, is used to reduce the size of the LTI models in this paper. The resulting reduced-order models are verified for open-loop and closed-loop fidelity against the full-order LTI model.

Model order reduction is first performed at the descending flight condition. Hankel singular values of the LTI system are plotted using a log-log scale in Fig. 6. The magnitude of the singular values decreases rapidly after the first 600 states. The last 2000 states have very small singular values, of the order of 10^{-15} and their contribution to the model's dynamic response is negligible. The pitching hub moment response to an open-loop flap deflection $\delta = 1^\circ \cos(4\psi + 90^\circ)$, predicted using three different reduced-order LTI models with 600, 400, and 200 states, respectively, is verified against the full-order LTI model in Fig. 7. All the hub shears and moments presented in this paper are non-dimensionalized using using M_b, L_b, and $1/\Omega$ for mass, length and time, respectively. The agreement between the full-order and reduced-order LTI models is excellent at 600 states but decreases as the number of states is reduced to 200. Therefore, the reduced-order LTI model approximation with 600 states is sufficient to capture all the relevant dynamics of the full order LTI model. A comparison of the various hub loads predicted using the full-order and the reduced-order LTI model with 600 states is shown in Fig. 8. The agreement between the full-order and the reduced-order LTI models is excellent in all the hub loads.

Similar open-loop verification is performed at a high-speed cruise condition with $\mu = 0.35$. Hankel singular values of the LTI system are plotted using a log-log scale in Fig. 9. Note that Fig. 9 is out of order and appears in the page before Fig. 8. As in the case of the lower advance ratio, the magnitude of the singular values decreases rapidly after the first 600 states. The pitching hub moment response to an open-loop flap deflection $\delta = 1^\circ \cos(4\psi + 90^\circ)$, pre-

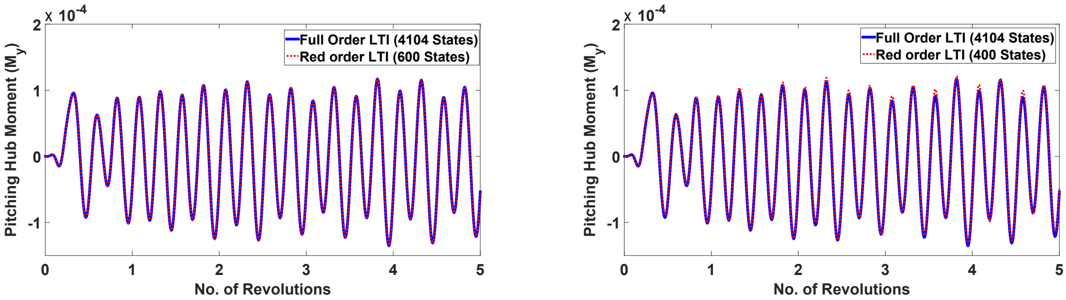

(a) 600 States

(b) 400 States

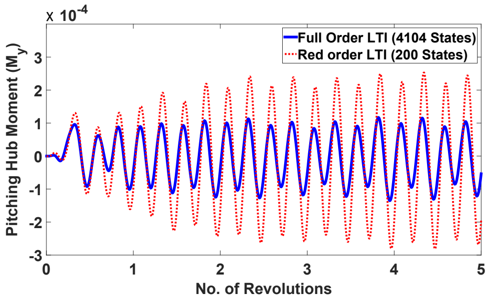

(c) 200 States

Figure 7: Open-loop verification of the pitching hub moment response obtained from various reduced-order LTI models against the full-order LTI model. $\mu = 0.15$, $\alpha_{\text{D}} = 6.5°$, and $\delta = 1° \cos(4\psi + 90°)$.

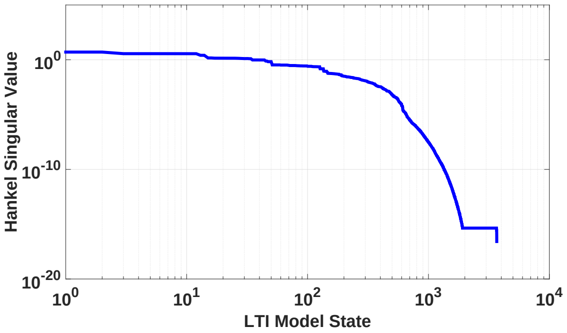

Figure 6: Hankel singular values for the full-order LTI model at $\mu = 0.15$.

dicted using three different reduced-order LTI models with 600, 400, and 200 states, respectively, is verified against the full-order LTI model in Fig. 10. The agreement between the full-order and reduced-order LTI models is excellent at 600 states but decreases as the number of states is reduced to 200. For the reduced-order model with 400 states, the error is large compared to the low advance ratio case. The presence of dynamic stall at high advance ratio requires the use of additional states for the same level of accuracy. The reduced-order LTI model approximation with 600 states is adequate for capturing the relevant dynamics in the full-order LTI model. A comparison of the various hub loads predicted using the full-order and the reduced-order LTI model with 600 states is shown in Fig. 11. The agreement between the full-order and reduced-order LTI models is excellent in all the hub loads.

In order to assess its closed-loop fidelity, the reduced-order LTI model extracted at the low-speed descending flight condition is implemented in the control loop shown in Fig. 3. First, the control sensitivity matrix used by the HHC controller is computed. Subsequently, the controller is engaged in closed-loop with the LTI model. The optimal flap deflections for vibration reduction predicted by the

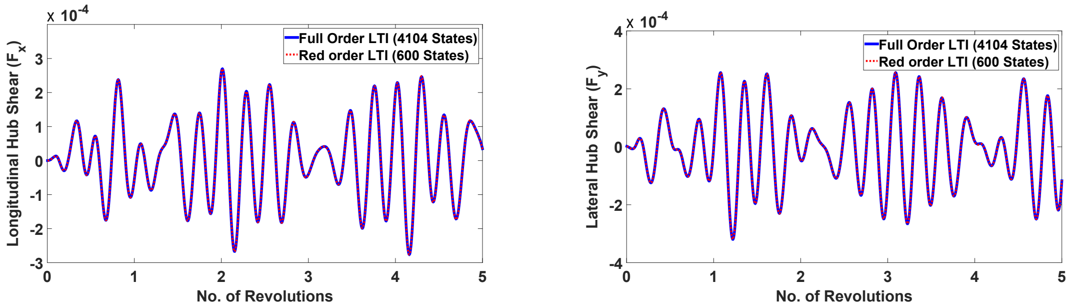

(a) Longitudinal hub shear (b) Lateral hub shear

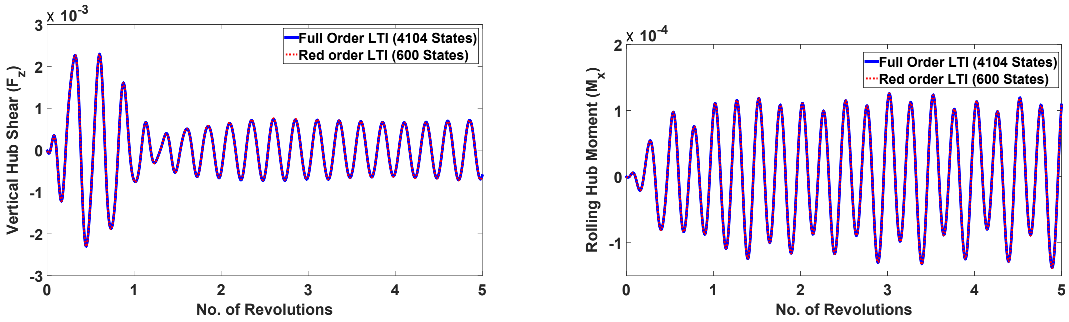

(c) Vertical hub shear (d) Rolling hub moment

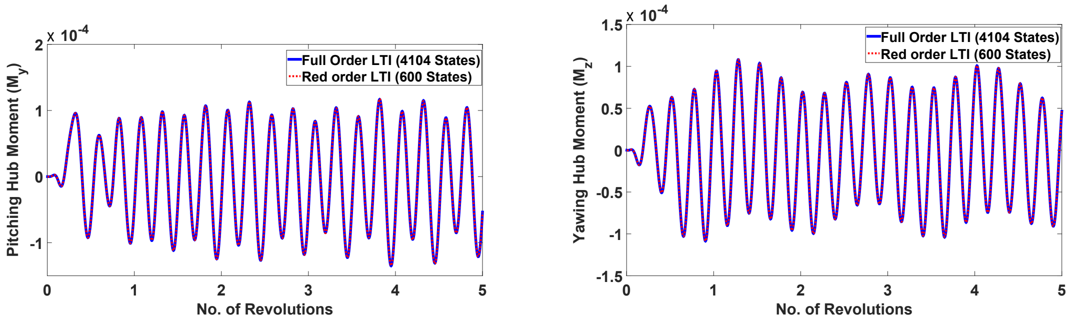

(e) Pitching hub moment (f) Yawing hub moment

Figure 8: Open-loop verification of the hub load response obtained from the reduced-order LTI model with 600 states against the full order LTI model. $\mu = 0.15$, $\alpha_{\text{D}} = 6.5^\circ$, and $\delta = 1^\circ \cos(4\psi + 90^\circ)$.

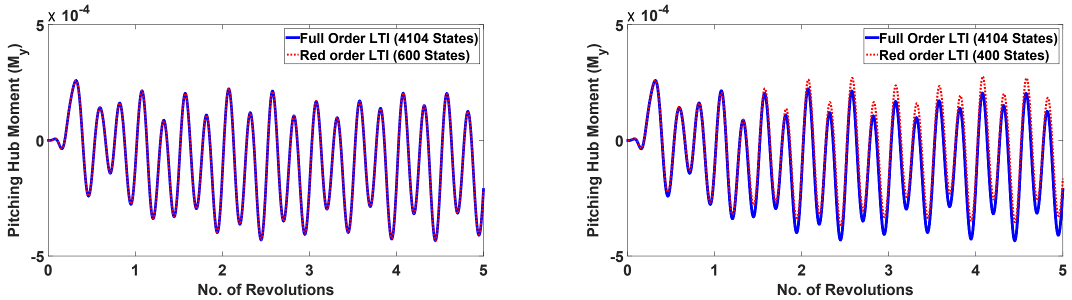

(a) 600 States (b) 400 States

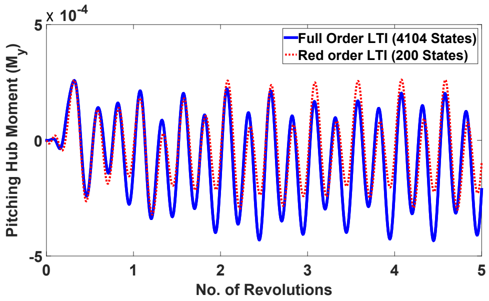

(c) 200 States

Figure 10: Open-loop verification of the pitching hub moment response obtained from various reduced-order LTI models against the full-order LTI model at a high-speed cruise condition. $\mu = 0.35$ and $\delta = 1^\circ \cos(4\psi + 90^\circ)$.

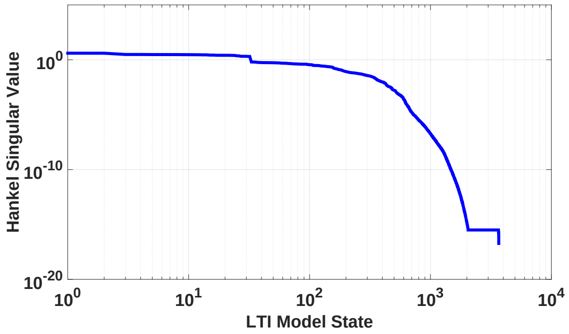

Figure 9: Hankel singular values for the full order LTI model at $\mu = 0.35$.

HHC controller when used in conjunction with the full-order LTI model, the reduced-order LTI model with 600 states, and the nonlinear model are compared in Fig. 12(a). The reduced-order model results are denoted in the legend as ‘LTI600Red’ whereas the full-order LTI model results are represented as ‘LTI’. The flap deflection consists of the 2/rev, 3/rev, 4/rev, and 5/rev harmonic components and the total flap deflection amplitude is limited to 1°. The flap deflection is limited to this value to account for actuator saturation using the algorithm described in Ref. 20. This limit on the flap deflection is refered to as the saturation limit. The flap deflection predictions based on the full-order and reduced-order LTI models agree very well. The two LTI model predictions agree reasonably well with the nonlinear model prediction, particularly in the magnitude and the azimuthal locations of the peaks and troughs. The differences in the predictions are quantified by a root mean square (RMS) error term defined as

$$(43) \quad E = \sqrt{(\Delta\delta_{2c}^2 + \Delta\delta_{2s}^2 + ... + \Delta\delta_{5c}^2 + \Delta\delta_{5s}^2)/8}.$$

Note that the harmonic components of the flap deflection presented here are the converged steady state

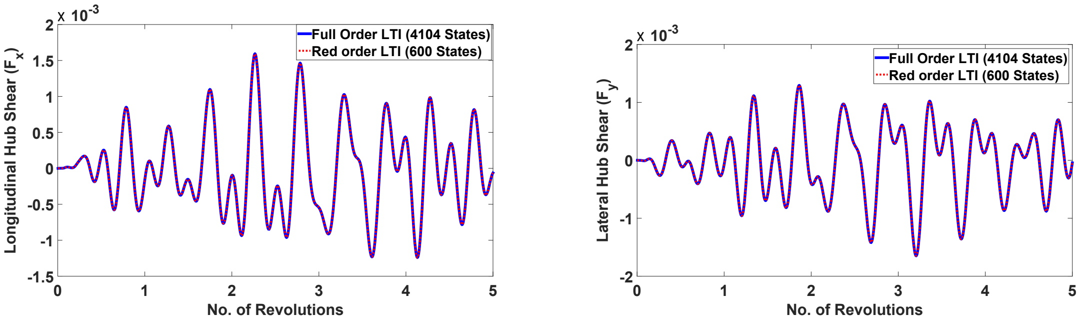

(a) Longitudinal hub shear (b) Lateral hub shear

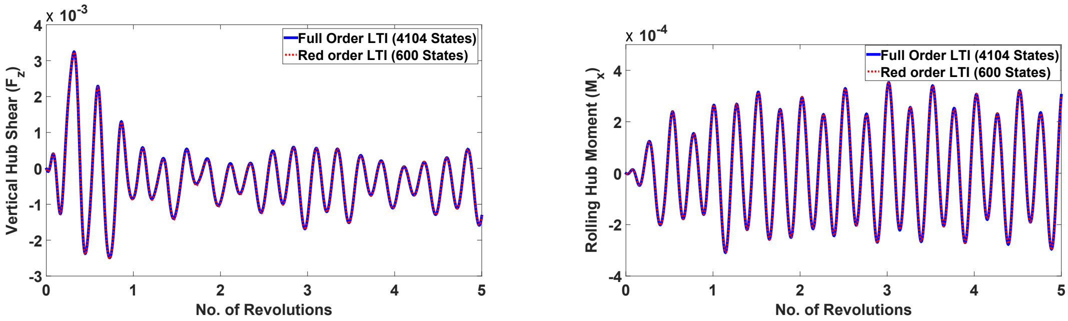

(c) Vertical hub shear (d) Rolling hub moment

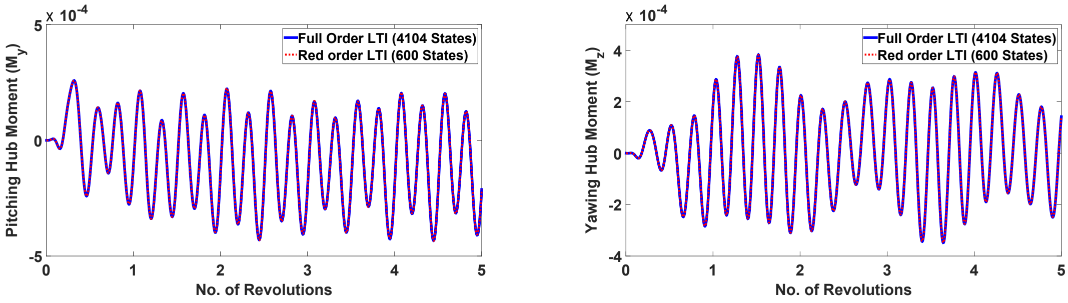

(e) Pitching hub moment (f) Yawing hub moment

Figure 11: Open-loop verification of the hub load response obtained from the reduced-order LTI model with 600 states against the full-order LTI model at a high-speed cruise condition. $\mu = 0.35$ and $\delta = 1^\circ \cos(4\psi + 90^\circ)$.

values. The RMS error between the full-order LTI model and nonlinear model flap predictions is 0.0022, whereas the RMS error between the reduced-order LTI model and the nonlinear model is 0.0019. The corresponding vibratory hub loads are compared to the baseline loads in Fig. 12(b). The reduced vibratory loads obtained using the nonlinear model and the two LTI models agree very well. Performance of the controller is evaluated based on the reduction achieved in the vibratory cost function

$$J = F_{HX4}^2 + F_{HY4}^2 + F_{HZ4}^2 + M_{HX4}^2 + M_{HY4}^2 + M_{HZ4}^2. \tag{44}$$

The nonlinear model yields a 24% reduction in the cost function compared to 34% obtained by the full-order LTI model and 37% obtained by the reduced-order LTI model. Thus, retaining 600 states in the LTI model is sufficient for enforcing closed-loop control fidelity.

Similar comparisons are performed for a maximum flap deflection limit of 2°. The optimal flap deflections predicted by the HHC controller used in closed-loop with the full-order LTI model, the reduced-order LTI model with 600 states, and the nonlinear model are compared in Fig. 13(a). The full-order and reduced-order LTI models show good agreement. The LTI model and nonlinear model based predictions agree reasonably well. There is good agreement in the magnitude of the peaks and troughs. However, their azimuthal locations show bigger errors compared to the 1° case. The RMS error between the full-order LTI model and nonlinear model flap predictions is 0.0063, whereas the RMS error between the reduced-order LTI model and the nonlinear model is 0.0054. The RMS error between the flap deflections predicted by the full-order and reduced-order LTI models is 0.0022. The corresponding vibratory hub loads are compared to the baseline loads in Fig. 13(b). The reduced vibratory loads obtained using the full-order and reduced-order LTI models agree reasonably well. The nonlinear model yields a 41% reduction in the cost function compared to 64% obtained by the full-order LTI model and 69% obtained by the reduced-order LTI model.

Linearized models extracted for cruise flight condition at $\mu = 0.35$ were also verified for closed-loop fidelity. The optimal flap deflections predicted by the HHC controller in conjunction with the full-order LTI model, the reduced-order LTI model with 600 states, and the nonlinear model are compared in Fig. 14(a). The flap deflection amplitude is restricted to 1°. The two LTI models show excellent agreement. The RMS error between the flap deflections predicted by the full-order and reduced-order LTI models is 0.00001. The RMS error between the predictions from the LTI models and nonlinear model is 0.0056. The corresponding vibratory hub loads are compared to the baseline loads in Fig. 14(b). The reduced vibratory loads obtained using the nonlinear model and the two LTI models agree reasonably well. The nonlinear model yields a 33% reduction in the cost function compared to 49% obtained by both the full-order and reduced-order LTI models. The full-order and reduced-order LTI models show excellent agreement but the agreement between the nonlinear and LTI models is not as good when compared to the low advance ratio case. These differences can be attributed to the presence of dynamic stall effects in the nonlinear model which are not captured by the LTI models. The dynamic stall model in AVINOR is based on an input relay function, that is, the model is activated only when the angle of attack is bigger than a predetermined value. Incorporating these nonlinear dynamic stall model characteristics into the LTI approximations requires significant modifications to the FEMR approach and will be considered in future studies.

7 Conclusions

Linearized time-periodic and time-invariant models capable of predicting the effects of on-blade control implemented by a plain trailing-edge flap were extracted from a high-fidelity nonlinear helicopter model, implemented in the AVINOR code. The model extraction was carried out at a low-speed descending flight, corresponding to BVI conditions, as well as high-speed cruise where DS effects are present. The size of the LTI models was excessive, in terms of the number of states, thus the models were computationally prohibitive in terms of cost. Therefore, a balanced model reduction method based on Hankel singular values was used to reduce the LTI model order. Fidelity of these reduced-order LTI models was verified by comparing their vibratory hub load response to open-loop flap deflection against that of the full-order LTI model and the nonlinear model. On-blade control is usually implemented in closed-loop mode, therefore, the reduced-order LTI models were also verified for closed-loop performance fidelity. The higher harmonic controller was used with a flap deflection that consists of a combi-

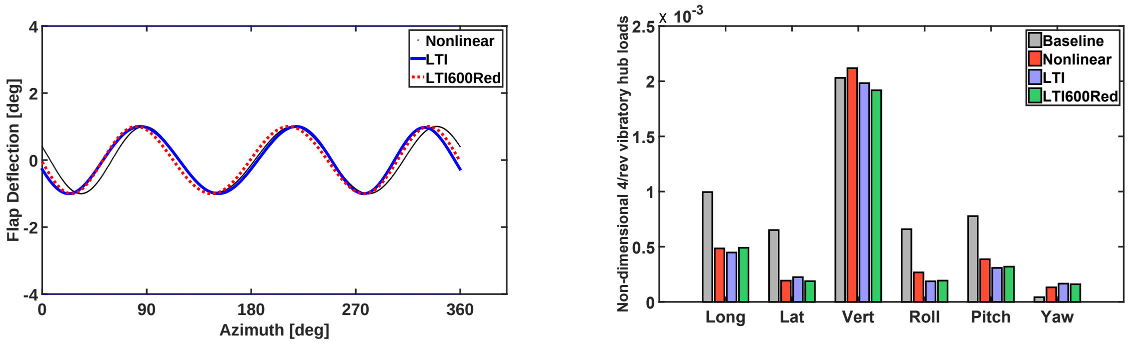

(a) Flap deflection

(b) Vibratory loads

Figure 12: Verification of the closed-loop flap deflection and vibratory loads obtained from the full-order LTI model and the reduced-order LTI model with 600 states against the nonlinear model. The flap deflection saturation limit is 1°. $\mu = 0.15$, $\alpha_{\mathrm{D}} = 6.5°$.

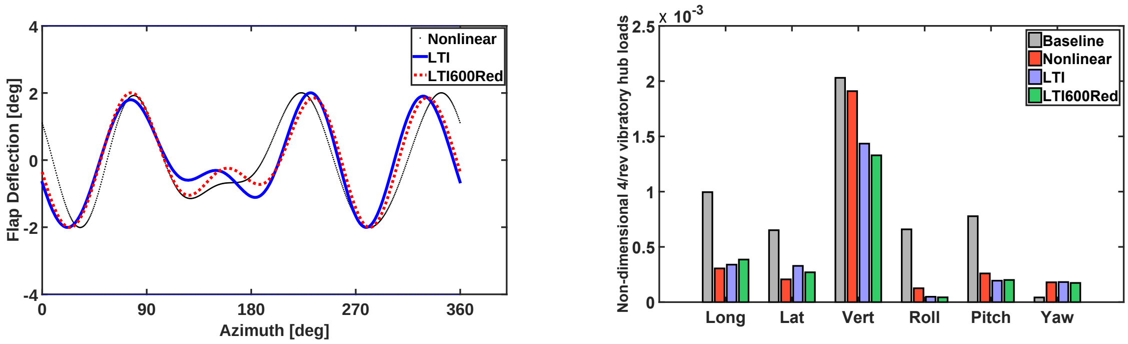

(a) Flap deflection

(b) Vibratory loads

Figure 13: Verification of the closed-loop flap deflection and vibratory loads obtained from the full-order LTI model and the reduced-order LTI model with 600 states against the nonlinear model. The flap deflection saturation limit is 2°. $\mu = 0.15$, $\alpha_{\mathrm{D}} = 6.5°$.

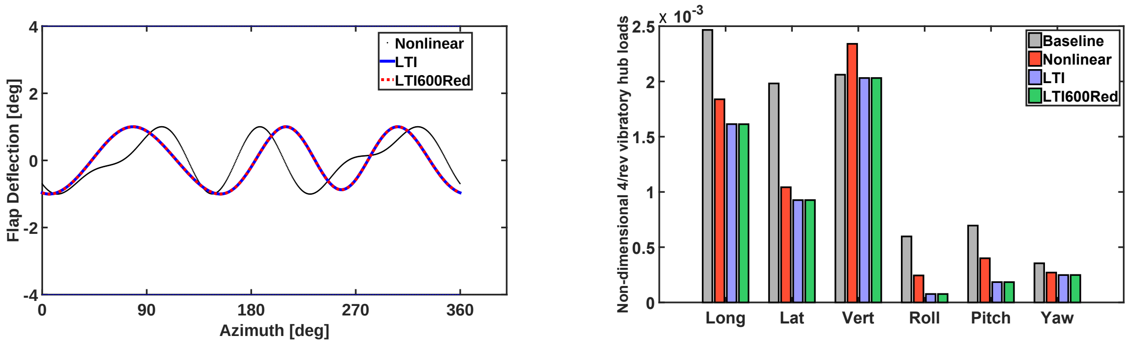

(a) Flap deflection

(b) Vibratory loads

Figure 14: Verification of the closed-loop flap deflection and vibratory loads obtained from the full-order LTI model and the reduced-order LTI model with 600 states against the nonlinear model. The flap deflection saturation limit is 1°. $\mu = 0.35$.

nation of 2, 3, 4, and 5/rev harmonic components as the control input and vibratory hub loads as the output. The principal conclusions are:

1. The Hankel singular value magnitudes of the full-order LTI models decrease rapidly after the first 600 states. Thus the size of the LTI models was reduced from 4104 to 600. This behavior was present at both the low-speed and high-speed flight conditions.
2. The vibratory hub load response to an open-loop 4/rev flap deflection predicted by the reduced-order LTI model was in excellent agreement with that predicted by the full-order LTI model. Reducing the number of states further down to 400 causes the agreement between the reduced-order and full-order LTI models to deteriorate. This deterioration was evident particularly at the high-speed flight condition.
3. For the closed-loop verification performed at a low-speed descending flight, the flap deflection predictions based on the reduced-order LTI, full-order LTI, and nonlinear models agree very well. For a 1° saturation limit on the flap deflection, the RMS error between the full-order LTI and nonlinear model flap deflections is 0.0022 whereas that between the reduced-order LTI and nonlinear models is 0.0019. A comparison of the corresponding vibratory hub loads indicates that the nonlinear model yields a 24% reduction in the vibratory cost function compared to 34% obtained with the full-order LTI model and 37% obtained with the reduced-order LTI model.
4. Increasing the flap deflection saturation limit to 2° increases the RMS error between the full-order LTI and nonlinear model flap deflections to 0.0063 and that between the reduced-order LTI and nonlinear models to 0.0054. The agreement between the flap deflections is still reasonable. The nonlinear model yields a 41% reduction in the cost function compared to 64% obtained with the full-order LTI model and 69% obtained by the reduced-order LTI model. As the flap deflection saturation limit is increased, the dynamics are forced further away from the operating condition and the small perturbation assumption is violated. Therefore, the errors between the linear and nonlinear model predictions are expected to increase.
5. Similar comparisons were performed at a cruise condition, $\mu = 0.35$, with the flap deflection saturation limit set to 1°. The full-order and reduced-order LTI models show excellent agreement in both the flap deflection and vibration reduction predictions. The LTI and nonlinear model predictions agree reasonably well. The RMS error between the LTI and noninear flap deflections is 0.0056. The nonlinear model yields a 33% reduction in the vibratory cost function whereas the both the LTI models yield 49% reduction. The agreement between the nonlinear and LTI models is not as good when compared to the low advance ratio case. These differences can be attributed to the presence of dynamic stall effects in the nonlinear model which are not captured by the LTI models. Incorporation of the nonlinear dynamic stall model characteristics into the LTI approximations will be considered in future studies.

Acknowledgments

This research was supported by the Vertical Lift Research Center of Excellence (VLRCOE) sponsored by NRTC and U.S. Army with Dr. M. J. Bhagwat as the grant monitor.

Copyright Statement

REFERENCES

1. Friedmann, P. P. , “On-Blade Control of Rotor Vibration, Noise, and Performance: Just Around the Corner?,” Journal of American Helicopter Society, Vol. 59, (4), July 2014, pp. 1–37.

2. Rabourdin, A. , Maurice, J. B. , Dieterich, O. , and Konstanzer, P. , “Blue Pulse Active Rotor Control at Airbus Helicopters - New EC145 Demonstrator and Flight Test Results,” Proceedings of the 70th American Helicopter Society Annual Forum, Montreal, Canada, May 2014.

3. Straub, F. K. , Anand, V. , Birchette, T. S. , and Lau, B. H. , “Wind Tunnel Test of the SMART Active Flap Rotor,” Proceedings of the 65th American Helicopter Society Annual Forum, Grapevine,TX, May 2009.

4. Padthe, A. K. , Liu, L. , and Friedmann, P. P. , “Numerical Evaluation of Microflaps for On Blade Control of Noise and Vibration,” Proceedings of the 52nd AIAA/ASME/ASCE/AHS/ACS Structures, Structural Dynamics and Materials Conference, Denver, CO, April 2011.

5. Padthe, A. K. , Friedmann, P. P. , and Prasad, J. V. R. , “High Fidelity Linear Time-Invariant Models for Rotor and Flight Control Interaction Studies,” Proceedings of the 5th Decennial AHS Aeromechanics Specialists’ Conference, San Francisco, CA, Jan 2014.

6. Padthe, A. K. and Friedmann, P. P. , “Closed-Loop Fidelity Assessment of Linear Time-Invariant Helicopter Models for Rotor and Flight Control Interaction Studies,” Proceedings of the 40th European Rotorcraft Forum, Southampton, UK, September 2014.

7. Anon., “Handling Qualities Requirements for Military Rotorcraft,” Aeronautical Design Standard-33 (ADS-33E-PRF), US Army Aviation and Missile Command, 2000.

8. Colaneri, P. , Celi, R. , and Bittanti, S. , “Constant-coefficient Representations of Periodic Coefficient Discrete Linear Systems,” Proceedings of the AHS 4th Decennial Specialist’s Conference on Aeromechanics, San Francisco, CA, Jan 2004.

9. Cheng, R. P. , Tischler, M. B. , and Celi, R. , “A High-Order, Time Invariant, Linearized Model for Application to HHC/AFCS Interaction Studies,” Proceedings of the 59th Annual Forum of the American Helicopter Society, Phoenix, AZ, May 2003.

10. Prasad, J. V. R. , Olcer, F. E. , Sankar, L. N. , and He, C. , “Linear Time Invariant Models for Integrated Flight and Rotor Control,” Proceedings of the 35th European Rotorcraft Forum, Hamburg, Germany, September 2009.

11. Abraham, M. D. , Olcer, F. E. , Costello, M. F. , Takahashi, M. D. , and Tischler, M. B. , “Integrated Design of AFCS and HHC for Rotorcraft Vibration Reduction Using Dynamic Crossfeeds,” Proceedings of the 67th Annual Forum of the American Helicopter Society, Virginia Beach, VA, May 2011.

12. Lopez, M. , Prasad, J. V. R. , Tischler, M. B. , Takahashi, M. D. , and Cheung, K. K. , “Simulating HHC/AFCS Interaction and Optimized Controllers using Piloted Maneuvers,” Proceedings of the 71st Annual Forum of the American Helicopter Society, Virginia Beach, VA, May 2015.

13. Glaz, B. , Friedmann, P. P. , Liu, L. , Kumar, D. , and Cesnik, C. E. S. , “The AVINOR Aeroelastic Simulation Code and Its Application to Reduced Vibration Composite Rotor Blade Design,” Proceedings of the 50th AIAA/ASME/ASCE/AHS/ACS Structures, Structural Dynamics and Materials Conference, Palm Springs, CA, May 2009. AIAA Paper No. 2009-2601.

14. Myrtle, T. F. and Friedmann, P. P. , “Application of a New Compressible Time Domain Aerodynamic Model to Vibration Reduction in Helicopters Using an Actively Controlled Flap,” Journal of the American Helicopter Society, Vol. 46, (1), January 2001, pp. 32–43.

15. Patt, D. , Liu, L. , and Friedmann, P. P. , “Simultaneous Vibration and Noise Reduction in Rotorcraft Using Aeroelastic Simulation,” Journal of the American Helicopter Society, Vol. 51, (2), April 2006, pp. 127–140.

16. Patt, D. , Liu, L. , Chandrasekar, J. , Bernstein, D. S. , and Friedmann, P. P. , “Higher-Harmonic-Control Algorithm for Helicopter Vibration Reduction Revisited,” Journal of Guidance, Control, and Dynamics, Vol. 28, (5), September-October 2005, pp. 918–930.

17. Hohenemser, K. H. and Yin, S. , “Some Applications of the Method of Multiblade Coordinates,” Journal of American Helicopter Society, Vol. 17, (3), July 1972, pp. 3–12.

18. Lopez, M. and Prasad, J. V. R. , “Fidelity of Reduced-Order Time-Invariant Linear (LTI)

Models for Integrated Flight and Rotor Control Applications," Proceedings of the 69th Annual Forum of the American Helicopter Society, Phoenix, AZ, May 2013.

19. Moore, B. , "Principal Component Analysis in Linear Systems: Controllability, Observability, and Model Reduction," IEEE Transactions on Automatic Control, Vol. AC-26, (1), Feb 1981, pp. 17–32.

20. Padthe, A. K. , Friedmann, P. P. , and Bernstein, D. S. , "Actuator Saturation in Individual Blade Control of Rotorcraft," Proceedings of the 53rd AIAA/ASME/ASCE/AHS/ACS Structures, Structural Dynamics and Materials Conference, Honolulu,HI, April 2012.